Solar Phys (2011) 273:1–13
DOI 10.1007/s11207-011-9846-y

Properties of Granules in Upflows and Downflows

Daren Yu · Zongxia Xie · Qinghua Hu · Shuhong Yang · Chunlan Jin

Received: 13 May 2009 / Accepted: 9 August 2011 / Published online: 12 October 2011

Abstract Normal-mode observations of seven quiet regions, obtained by the *Hinode* spacecraft, are used to analyze the physical properties of granules with mean upward and downward Doppler velocity. We identify 75 146 granules from the observations with a granule-detection method. Then the granules are divided into two subsets: one with negative mean Doppler velocity (granule-upflows), and the other with positive mean Doppler velocity (granule-downflows). Next, the statistical properties and distributions of these two subsets of granules are measured and discussed. We also study the relation between the Doppler velocity of granules and other properties.

Several conclusions are drawn from the statistical analysis: *i*) The majority (73.5%) of granules have negative mean Doppler velocity (blueshift). *ii*) The continuum-intensity distribution of granule-upflows reaches a peak at 1.05, while that of granules-downflows reaches a peak at 0.99. *iii*) Granule-upflows are greater than granule-downflows if transverse, absolute longitudinal and unsigned flux density are smaller than 100 G, while granule-upflows are less than granule-downflows if the flux densities are greater than 100 G. *iv*) Granule-downflows are – on average – slightly smaller and fainter than granule-upflows. Also, the flux densities of granule-downflows are slightly higher. *v*) The mean Doppler velocity within intergranular lanes is the most highly correlated with that within granules among the eight properties of granules.

Keywords Granulation · Magnetic fields · Photosphere

D. Yu · Z. Xie (✉) · Q. Hu
Harbin Institute of Technology, Harbin 150001, China
e-mail: caddiexie@hotmail.com

S. Yang · C. Jin
Key Laboratory of Solar Activity, National Astronomical Observatories, Chinese Academy of Sciences, Beijing 100012, China

S. Yang
e-mail: shuhongyang@ourstar.bao.ac.cn

1. Introduction

Solar granulation is visible as the manifestation of convective motions on the Sun. It is a cellular pattern of bright elements (granules) surrounded by darker intergranular lanes. Research of granulation can help to understand the activity of the Sun.

The velocity distribution and range of granules have been studied by many researchers. The distribution of granular velocity in units of pixels is skewed (Keil and Canfield, 1978; Hirzberger, 2002). The slopes toward negative velocities are significantly steeper than toward positive velocities. With *Hinode* data, the distribution of granular Doppler velocity was studied by Jin, Wang, and Zhao (2009). Their statistical analysis showed that the granular motion ranged from $-3.3\ \mathrm{km\,s^{-1}}$ (blueshift) to $2.0\ \mathrm{km\,s^{-1}}$ (redshift) with a peak at $-1.0\ \mathrm{km\,s^{-1}}$.

The velocity distributions within granules have also been studied. Rast (1995) pointed out that regions of maximum granular upflow do not lie at the centers of the granules but along their edges, immediately adjacent to the intergranular downflow lanes. Hirzberger (2002) also found that the intensity and velocity distribution within the granules depends on the granular size. In smaller structures the maximum intensities and velocities are located closer to the granular barycenters, whereas for larger granules the maxima are shifted toward the granular boundaries.

It has been shown that the granules in different regions have different properties. Brandt *et al.* (1991) showed that small, faint, and rapidly collapsing granules are located preferentially in the negative divergence regions of the mesogranular flow field, while bright, long-lived, and rapidly expanding granules populate preferentially the positive-divergence regions. Hirzberger *et al.* (1997) found that the large and small granules are unevenly distributed with respect to the large-scale vertical flows. Smaller granules are more concentrated along downdrafts, whereas larger ones preferentially occupy the updrafts.

Moreover, the velocities in granular upflows are anticorrelated with the velocities in their surrounding lanes (Stein and Nordlund, 1998; Rast 1995, 2003). Using *Hinode* data, Jin, Wang, and Zhao (2009) also found that there is a negative correlation between Doppler velocity and the continuum intensity. Namely, the larger the spectral blueshift, the brighter the granule.

The vector magnetic fields of granules in different regions are poorly studied because of the limitation by the spatial resolution and sensitivity of polarization measurements. Observations of the quiet Sun from the *Solar Optical Telescope/Spectro-Polarimeter* (SOT/SP) on the *Hinode* spacecraft provide a new opportunity to advance our knowledge on the interaction between the magnetic field and granulation. With *Hinode* data, Lites *et al.* (2007) found that the quiet internetwork regions are pervaded by horizontal magnetic flux. The spatial-average horizontal apparent flux density is 55 G, and the corresponding average vertical apparent flux density is 11 G. They also found that the vertical fields are concentrated in the intergranular lanes, whereas the stronger horizontal fields occur most commonly at the edges of the bright granules (Lites *et al.*, 2007, 2008). Jin, Wang, and Zhao (2009) analyzed the vector magnetic fields of granules with *Hinode* data.

In this article, we identify 75 146 granules with a granule-detection method. Then the granules are separated into two subsets according to their mean Doppler velocity. The properties of these two subsets are studied. The relationship between the Doppler velocity and other properties of granules is also analyzed.

Section 2 describes the observations and the automatic granule-detection method. In Section 3, we analyze the properties of granule-upflows and granule-downflows, respectively. The quantitative relations between Doppler velocity of granules and other proper-

ties are measured in Section 4. Sections 5 and 6 give a discussion and conclusion, respectively.

2. Observations and Automatic Granule-Detection Method

Seven quiet regions located near the disk center were used. They were taken with the SOT (Suematsu *et al.*, 2008; Shimizu *et al.*, 2008; Ichimoto *et al.*, 2008; Tsuneta *et al.*, 2008) instrument on *Hinode* (Kosugi *et al.*, 2007). The SP (Lites *et al.*, 2001) in *Hinode*/SOT provides the full Stokes profiles of two Fe lines at 630.15 nm and 630.25 nm in four modes (normal, fast, dynamics, and deep maps). The SP maps adopted here were observed in the normal map mode. For each raster slit, the integrated exposure time is 4.8 seconds and the pixel sampling along the slit is $0.16''$. The scan is in the east – west direction with the scanning step of about $0.1476''$. Each slit requires 4.8 seconds, so a single $2''$ granule can be mapped in about one minute which is shorter than six minutes, the typical evolution time of granules (Bahng and Schwarzschild, 1961; Title, Tarbell, and SOUP Team, 1986). Therefore, we assume that we can use such a map to characterize a granule as if it were a snapshot.

The Stokes spectrum inversion technique based on the assumption of Milne–Eddington atmospheres (T. Yokoyama, private communication, 2009) is an effective means to derive vector magnetic fields. The inversion returns the values of 13 physical parameters including the vector magnetic field (magnetic strength $[B]$, the magnetic inclination $[\gamma]$, and the magnetic azimuth $[\phi]$), the stray-light fraction α, the Doppler velocity, and some other parameters. The stray-light intensity profile is calculated by assuming that the vector magnetic fields is zero in the Milne–Eddington atmosphere. The vector magnetic field $[B]$ is shown with the longitudinal field $[(1-\alpha)B\cos\gamma]$ and the transverse field $[(1-\alpha)^{1/2}B\sin\gamma]$, where α is the non-magnetic fraction of the atmosphere, $(1-\alpha)$ is the magnetic filling factor, and γ is the inclination angle corresponding to the line-of-sight direction. The Doppler shifts are derived from the Fe I 630.25 nm Stokes I profiles and averaged over the whole field-of-view. We only analyzed the pixels with total polarization degree above the noise level of $1.0\times10^{-3}I_{\rm c}$ in the polarization continuum. So the pixel values which are less than the noise level are set to zero before inversion. Information about the data sets is presented in Table 1.

Before statistical analysis, we detect the granules from the observations. Several algorithms for segmenting solar-granulation images have been developed. A review of existing segmentation algorithms was presented by Berrilli *et al.* (2005). They applied a multi-scale Laplacian-of-Gaussian operator and an iterative version of Medial Axis Transform as tools

Table 1 Data sets

Date	Field of view	Start time (UT)	End time (UT)
24 Nov. 2006	$302.14''\times162.30''$	20:32:10	23:25:48
16 Jan. 2007	$268.48''\times162.30''$	11:22:07	13:56:30
10 Mar. 2007	$302.14''\times162.30''$	11:37:36	14:36:48
16 Apr. 2007	$147.60''\times162.30''$	00:23:23	01:48:11
15 Oct. 2007	$268.63''\times162.30''$	17:21:49	19:56:18
13 Nov. 2007	$151.14''\times162.30''$	15:39:05	17:05:55
21 Dec. 2007	$151.14''\times162.30''$	00:20:44	01:47:33

for the segmentation of granules and granular cells. Roudier and Muller (1987) used a single threshold to retrieve the granular structures after enhancing the spatial scale and filtering some noises. In the present study it is not feasible to apply such a method, as the parameters of the filter, as well as the threshold, must be found by trial and error. This would give rise to a lack of confidence in the statistical results. To recognize the boundaries of both solar granular and supergranular cells, Schrijver and Hagenaar (1997) used the watershed-transform method. The advantage of this approach is the absence of a chosen threshold. However, the watershed transform may lead to over-segmentation due to noise or local irregularities in the image if these are not removed with a suitable low-pass filter. Bovelet and Wiehr (2001) developed a multiple-level tracking algorithm, which is superior to commonly used Fourier-based recognition techniques. However, the selection of the different intensity levels makes the method very difficult to apply to the present images.

In this article, we introduce the technique of a marker-controlled watershed to recognize the granules (Moga and Gabbouj, 1998). This method is generalized from the watershed method, which is a popular segmentation method for separating touching or adjacent objects. Watershed is a region-growing algorithm taking an image as a topographic surface (Meyer and Beucher, 1990), and the segmentation algorithm is viewed as a flooding process. If we consider the image as a topographic relief, where the height of each point is directly related to its gray level and rain gradually falls on the terrain, the watersheds are the lines that separate the "lakes" (actually called catchment basins). Contacting points between the propagation originating from different minima are defined as the boundaries of the regions and are used to create the final partition. Generally, the watershed transform is computed on the gradient of the original image, so that the catchment-basin boundaries are located at high-gradient points.

However, it has been reported that the watershed algorithm often leads to over-segmentation in Salembier and Pardas (1994). Namely, the method may divide one large granule into a set of small granules. Markers are used to overcome this problem (Salembier and Marques, 1999). A marker is a connected component in an image. Internal markers are associated with the objects of interest, while external markers are associated with the background. If we get some markers, the image is smoothed to ensure that only these markers are local minima. Then we use the watershed method on the smoothed image. The image can be segmented to isolated granules, and each marker indicates the presence of a granule. A typical procedure of the marker-controlled watershed method consists of five steps (Yu *et al.*, 2011):

i) Deriving the gradient image. The gradient image is the derivative of the local image values. An edge in the original image will correspond to a greater value in the gradient image. We use the Sobel operator to get the gradient image $[G]$. There are two kernels which are convolved with the original image $[I]$ to compute the gradients in the horizontal and vertical directions, $[G_x]$ and $[G_y]$. Then the result of convolutions are combined as

$$|G| = \sqrt{G_x^2 + G_y^2},$$

where

$$G_x = \begin{bmatrix} -1, & 0, & 1 \\ -2, & 0, & 2 \\ -1, & 0, & 1 \end{bmatrix} * I, \qquad G_y = \begin{bmatrix} +1, & +2, & +1 \\ 0, & 0, & 0 \\ -1, & -2, & -1 \end{bmatrix} * I,$$

and $*$ denotes the two-dimensional convolution operation. The gradient image is shown in panel (b) of Figure 1 (Yu *et al.*, 2011):

ii) Obtaining the markers of continuum image. As there is some noise in the image, we first use the lift-wavelet transform (Sweldens, 1998) and two-dimension Wiener filter (Lim, 1990) to smooth the image. These two filters can enhance the contrast of an image. Then eroding (Boomgaard and Balen, 1992) is used to thin the connected parts to get the marker of each granule. The markers are white in panel (d) of Figure 1.

iii) Smoothing the gradient image using the derived markers. This step is used to modify the gradient image so that its local minima are only in the marked locations. Morphological function reconstruction is used to smooth the gradient image (Rivest, Soille, and Beucher, 2005).

iv) Obtaining the segmentation result of granules. Watershed is a region-growing algorithm. Each granule starts from its mark, which is the local minimal point, and stops at certain thresholds, which are the local maximal points around the mark. Because watershed is used on the smoothed gradient image, the boundary we found is the local maximal gradient. Therefore, the granules are separated from their surrounding lanes by the boundaries. The result is shown in panel (e) of Figure 1, where the original image is overplotted by the boundaries.

v) Obtaining the segmentation result of granular cells. Here, granular cells are defined as the granular elements including one-half of the surrounding dark lanes. First, we use the result from step *iv*) to get a binary image. The pixels identified as granules are set to zero, while the other pixels are set to one. Then watershed is applied again to this binary image. Therefore, the surrounding dark lanes are divided equally between the neighboring granules and we get the granular cells. The result is given in panel (f) of Figure 1.

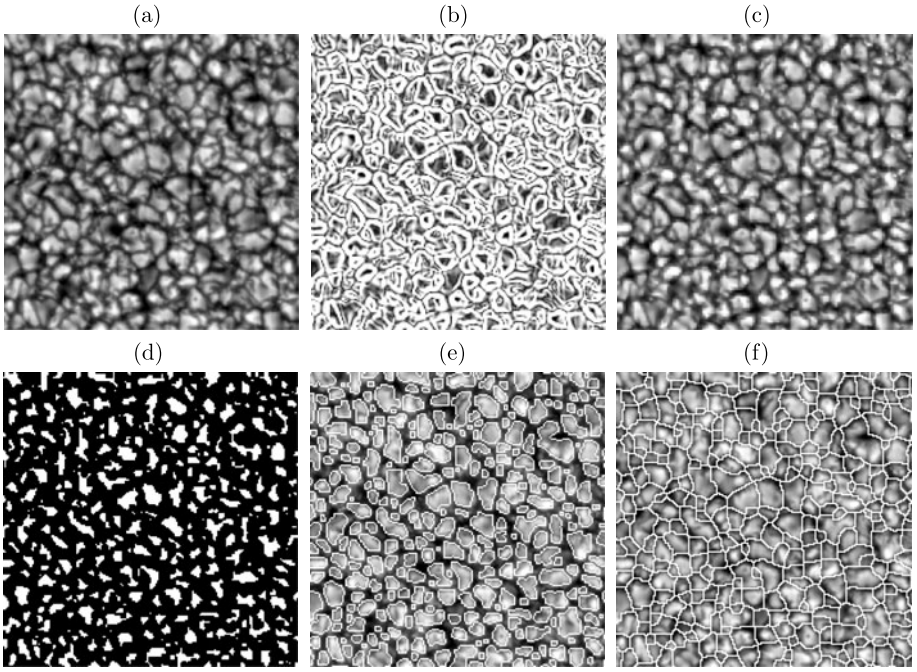

Figure 1 Procedure of granule recognition algorithm. (a) A part of original continuum image, (b) gradient image, (c) smoothed image, (d) marked image, (e) segmented image, (f) segmented cell image.

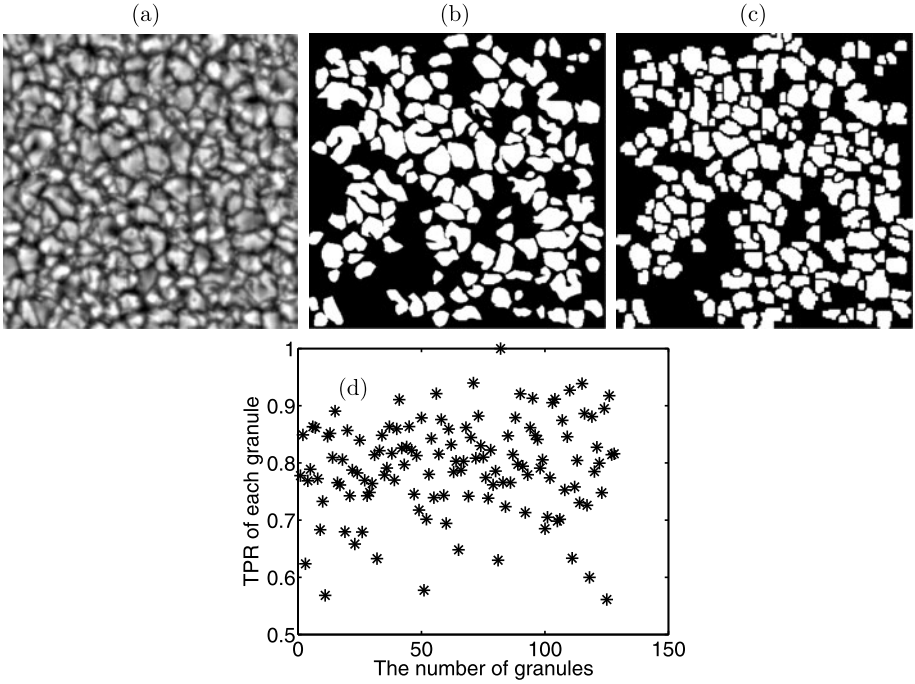

Figure 2 Quantitative evaluation of our method. (a) Part of original continuum image, (b) 128 granules found by hand, (c) segmented results by our method, (d) true positive rate (TPR) of 128 granules.

To quantitatively evaluate the given method, we manually label 128 granules in the continuum image and take them as ground truth. Next, we compute the true positive rate (TPR) for the segmentation results (Ning *et al.*, 2010). The TPR is defined as the ratio of the number of correctly classified pixels to the number of total pixels of each granule in the ground truth. Obviously, the higher the TPR is, the better the method is. Figure 2 shows these results. The mean value of TPR is 0.79, which is not very high because some small granules found by our method are recognized as a single one by hand. However, these small granules can be recognized as individual from the original continuum image of Figure 2a.

From the seven quiet regions listed in Table 1, a total of 75 825 granules are identified with the above method. However, the flux densities of some granules are even higher than 800 G. They may be network bright points. According to the statistical results of Jin, Wang, and Zhao (2009), the absolute longitudinal-flux densities of granules are between 0 and 212 G. So the granules with absolute longitudinal-flux density higher than 300 G are removed. There are 75 146 granules left.

We briefly describe the data and the parameters used to characterize the granulation here. Granules are the granular pattern excluding the surrounding intergranular lanes. Granular cells are defined as the granular elements including one-half of the surrounding dark lanes. To describe the properties of granules, we define the following parameters: *i*) Granule diameter is derived from its area [A] through the relation $\sqrt{4A/\pi}$. *ii*) Continuum intensity, Doppler velocity, absolute longitudinal-flux density, transverse-flux density, unsigned-flux density, and inclination of granules are the mean intensity, the mean Doppler velocity, the mean absolute longitudinal-flux density, the mean transverse-flux density, the mean unsigned-flux density, and the mean inclination within the granules, respectively. *iii*) Doppler velocity of

lanes is the mean Doppler velocity within the half intergranular lanes around the granules excluding the boundary of cell. *iv*) Granule-upflows are the granules with the mean negative Doppler velocity. *v*) Granule-downflows are the granules with the mean positive Doppler velocity.

3. Results and Analysis

In this section, scatter plots of granular diameter, continuum intensity, and vector magnetic fields *versus* Doppler velocity are first analyzed. We find some qualitative rules from these plots. Then the Doppler-velocity distribution of granules is given. Finally, to analyze the different physical properties of granules in downflows and upflows, we separate the granules into two subsets: 55 226 (73.5%) granules with mean negative Doppler velocity (blueshift; granule-upflows) and 19 920 (26.5%) granules with mean positive Doppler velocity (redshift; granule-downflows), respectively. The statistical properties and distributions of these two subsets of granules are measured.

Figure 3 shows the scatter plots of granular diameter, continuum intensity, vector magnetic fields, and Doppler velocity of lanes *versus* mean Doppler velocity of granules. It is easy to see that granule-downflows have a smaller diameter and continuum intensity, but

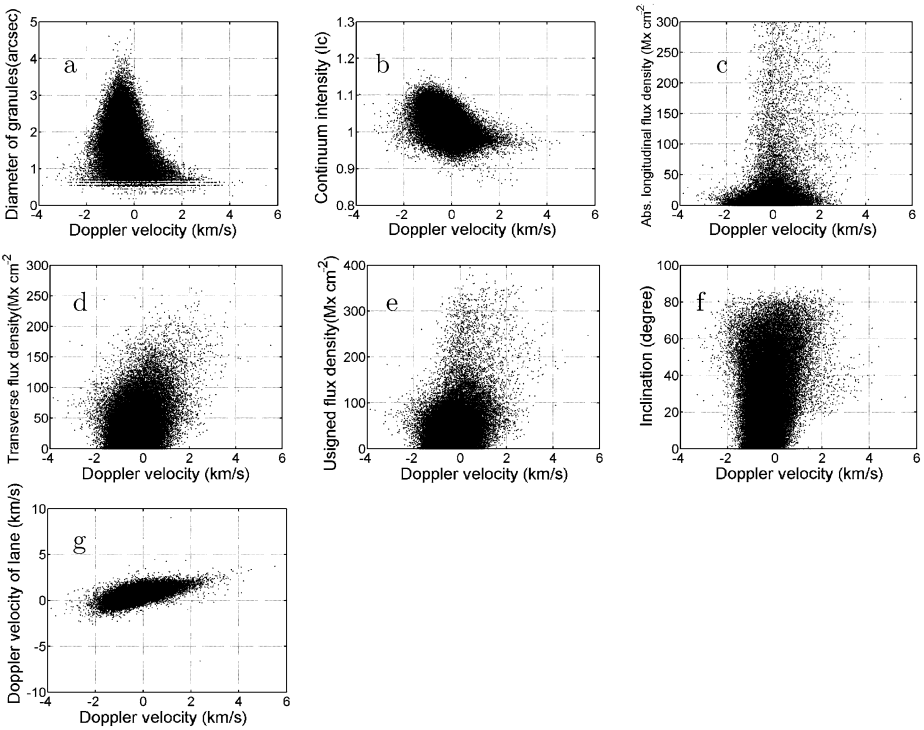

Figure 3 Scatter plots of some granular properties *vs.* granular mean Doppler velocity. (a) Diameter of granules *vs.* velocity of granules, (b) mean continuum intensity *vs.* velocity of granules, (c) absolute longitudinal-flux density *vs.* velocity of granules, (d) transverse-flux density *vs.* velocity of granules, (e) unsigned flux density *vs.* velocity of granules, (f) magnetic inclination *vs.* granular velocity, (g) Doppler velocity of lanes *vs.* velocity of granules.

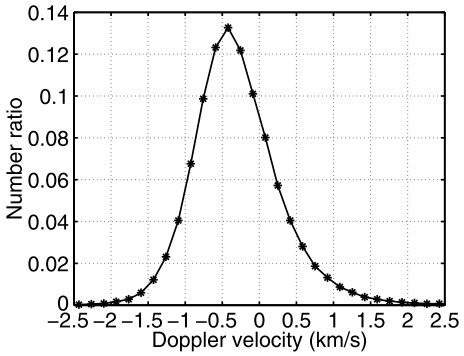

Figure 4 The mean Doppler velocity distribution of all granules.

Table 2 The properties of granules in downflows and upflows.

	Term	Average	Standard	Range
Granule-downflows	Mean velocity [km s^{-1}]	[0.46	0.47	[0,1.87]
	Velocity of lane [km s^{-1}]	0.95	0.52	[−0.61,2.51]
	Diameter [″]	1.12	0.46	[0.18,2.50]
	Continuum intensity [I_c]	1.00	0.03	[0.91,1.09]
	Transverse-flux density [G]	47.83	41.80	[0.00,173.2]
	Abs. longitudinal density [G]	18.65	41.54	[0.00,143.3]
	Unsigned-flux density [G]	55.17	57.91	[0.00,228.9]
	Inclination [degrees]	32.54	21.46	[0.00,88.53]
Granule-upflows	Mean velocity [km s^{-1}]	−0.57	0.37	[−1.68,0)
	Velocity of lane [km s^{-1}]	0.35	0.49	[−1.12,1.82]
	Diameter [″]	1.67	0.63	[0.18,3.56]
	Continuum intensity [I_c]	1.03	0.03	[0.94,1.12]
	Transverse-flux density [G]	25.65	27.06	[0.00,106.8]
	Abs. longitudinal density [G]	5.89	18.24	[0.00,60.6]
	Unsigned-flux density [G]	27.71	32.88	[0.00,126.3]
	Inclination [degrees]	21.34	19.23	[0.00,86.73]

larger absolute longitudinal, transverse, and unsigned-flux density. The relationship between the Doppler velocity of lanes and that of granules is approximately linear.

The distribution of granular Doppler velocity is shown in Figure. 4. The distribution is skewed with the mean value -0.29 km s^{-1} and the standard deviation 0.61 km s^{-1}. It reaches a peak at -0.42 km s^{-1}. This result is consistent with the velocity distribution of pixels in previous work (Keil and Canfield, 1978; Hirzberger, 2002). The slope toward negative velocities is significantly steeper than the slope toward positive velocities.

Table 2 shows the statistical properties of granule-downflows and granule-upflows. The average [μ], standard deviation [σ], and range of each property are given. To reduce the influence of outliers, the range of each property in Table 2 is computed by $\mu - 3\sigma$ and $\mu + 3\sigma$. Therefore, the range of granular diameter is between 0.18″ and 3.56″. And there are only 124 granules (0.17%) with a diameter larger than 3.56″. The range of mean Doppler velocity of intergranular lanes is between -1.12 km s^{-1} and 2.51 km s^{-1}. There are only 0.39%

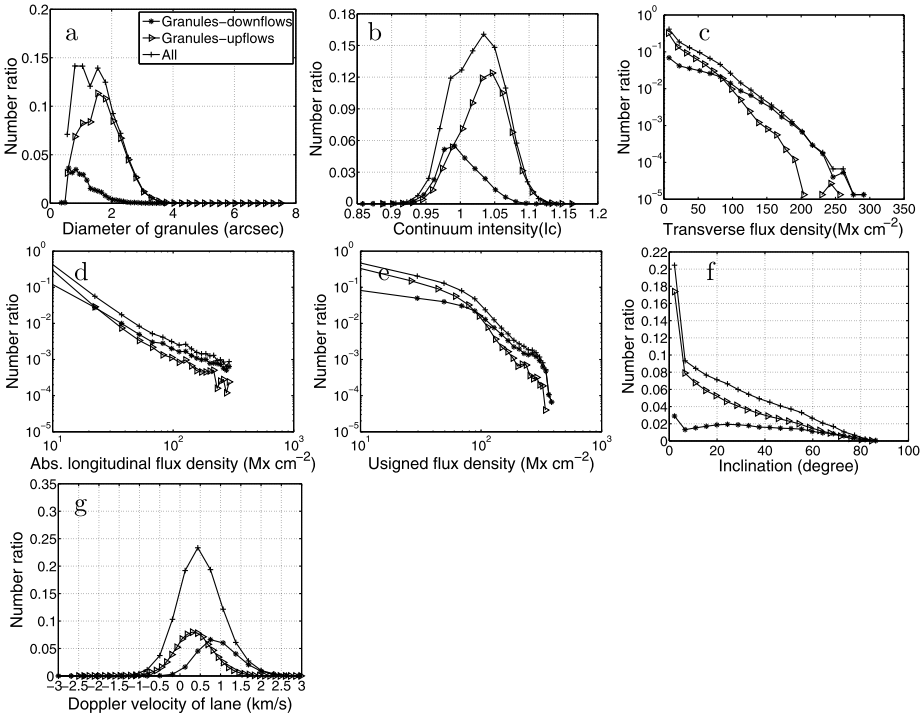

Figure 5 The normalized distributions of properties of all granules are shown by pluses, granule-downflows are shown by asterisks, and granule-upflows are shown by triangles. Normalization is achieved by dividing each distribution by the total number of granules: 75 146.

of granules out of the above range. The mean Doppler velocity of granule-downflows ranges from 0 km s^{-1} to 1.87 km s^{-1}, and the mean value is 0.46 km s^{-1}, while that of granule-upflows is between -1.68 km s^{-1} and 0 km s^{-1} with the mean value of -0.57 km s^{-1}.

We can see that the averages and ranges of the diameter of granule-downflows are a little smaller than those of granule-upflows in Table 2. The mean diameter of granule-downflows is 1.12″, and the range is [0.18″, 2.50″], while the mean diameter of granule-upflows is 1.67″, and the range is [0.18″, 3.56″]. The diameter distributions of these two parts in panel (a) of Figure 5 show that granule-upflows are more than granule-downflows in each scale of diameter.

We also give the averages and ranges of continuum intensity of granule-downflows and granule-upflows in Table 2. The average of mean continuum intensity of granule-downflows is 1.00, which is a little smaller than the 1.03 of granule-upflows. The ranges of these two parts are close to each other, [0.91, 1.09] and [0.94, 1.12], respectively. However, the continuum-intensity distribution of granule-downflows reaches a maximum of 0.99, while that of granule-upflows reaches a peak at 1.04, as shown in panel (b) of Figure 5. Moreover, granule-downflows are more than granule-upflows if continuum intensity is smaller than 0.99. If continuum intensity is higher than 0.99, granule-downflows are less than granule-upflows.

The averages of transverse, absolute longitudinal, unsigned-flux density, and inclination of granule-downflows are all larger than those of granule-upflows, although the ranges of these properties of the two components are close. The distributions of these properties of

the two components are shown in panels (c, d, e, f) of Figure 5, respectively. Granule-upflows are higher in number than granule-downflows if transverse, absolute longitudinal, and unsigned flux densities are smaller than 100 G, while granule-upflows are fewer than granule-downflows if the flux densities are higher than 100 G. However, there are more granule-upflows than granule-downflows in each scale of inclination.

From Table 2, we know that the average Doppler velocity of lanes surrounding granule-downflows is 0.95 $\mathrm{km\,s^{-1}}$ and the average of those surrounding granule-upflows is 0.35 $\mathrm{km\,s^{-1}}$, while the range of Doppler velocity of lanes around granule-downflows is wider than the range around granule-upflows. From panel (g) of Figure 5, we get the Doppler velocity distributions of all lanes. The lanes around granule-upflows, and the lanes around granule-downflows reach peaks at 0.44 $\mathrm{km\,s^{-1}}$, 0.30 $\mathrm{km\,s^{-1}}$, and 0.75 $\mathrm{km\,s^{-1}}$, respectively. Granule-upflows are more than granule-downflows if the Doppler velocity of the lane is smaller than 0.6 $\mathrm{km\,s^{-1}}$.

4. Relation between Granular Properties and Doppler Velocity

The relation between Doppler velocity and other properties of granules may be linear or nonlinear. So we introduce two coefficients widely used in relevance analysis to measure the linear and nonlinear relations.

Pearson's correlation coefficient is widely used to measure the linear relation between two random variables. Given two random variables $X = \{X_1, X_2, \ldots, X_m\}$ and $Y = \{Y_1, Y_2, \ldots, Y_m\}$, the correlation coefficient is computed as

$$S(X, Y) = \frac{\sum_{i=1}^{m} (X_i - \overline{X})(Y_i - \overline{Y})}{\sqrt{\sum_{i=1}^{m} (X_i - \overline{X})^2 \sum_{i=1}^{m} (Y_i - \overline{Y})^2}} ,$$

where $\overline{X}$ and $\overline{Y}$ are the average values of X and Y, respectively.

We compute the correlation coefficients between the properties of granules and Doppler velocity of granules [V_g]. The linear correlation coefficients between continuum intensity [I_c], diameter [G_g], transverse-flux density [B_t], absolute longitudinal-flux density [$|B_\mathrm{l}|$], signed longitudinal-flux density [B_l], unsigned-flux density [B], magnetic inclination [I_n], Doppler velocity of lane [V_l], and Doppler velocity of granules are −0.48, −0.36, 0.32, 0.26, 0.01, 0.32, 0.20, and 0.61, respectively. We can see that Doppler velocity of lanes [V_l] has the greatest correlation to Doppler velocity of granules. This conclusion is consistent with the analysis in the above section. Continuum intensity [I_c] is the second greatest one, followed by granular diameter [D_g], transverse-flux density [B_t], and unsigned flux density [B].

Meanwhile, we also use mutual information to characterize the nonlinear relevance between the eight granular properties and Doppler velocity of granules. Given two random variables X and Y, the probability distributions are denoted by $p(x_i)$ and $p(y_i)$. Then the entropies of random variables X and Y are (Battiti, 1994):

$$H(X) = -\sum_{i=1}^{m} p(x_i) \log p(x_i), \qquad H(Y) = -\sum_{i=1}^{m} p(y_i) \log p(y_i) .$$

The mutual information between X and Y is computed as

$$MI(X, Y) = H(X) + H(Y) - H(XY),$$

where $H(XY)$ is the joint entropy of the two variables.

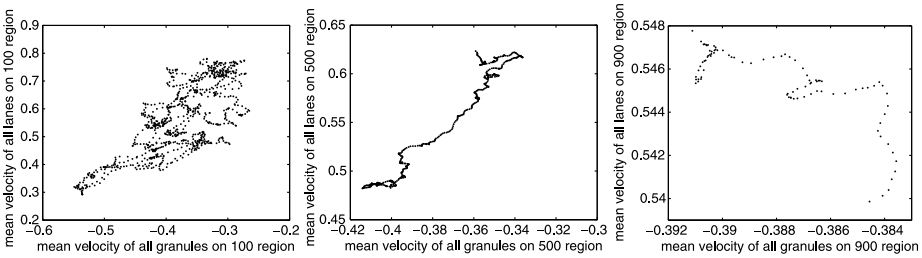

Figure 6 Relation of the mean velocities of granules and lanes in square regions of 100×100, 500×500, and 900×900 pixels.

Mutual information between two random variables reflects the degree of nonlinear relevance. We compute the mutual information between the eight properties and Doppler velocity of granules. The mutual information between I_c, G_g, B_t, $|B_l|$, B_l, B, I_n, V_l, and V_g are 0.14, 0.13, 0.06, 0.06, 0.06, 0.06, 0.05, and 0.18, respectively. Therefore, the mutual information between $[V_l]$ and $[V_g]$ is the greatest among the eight values, followed by $[I_c]$ and $[D_g]$. The result shows that $[V_l]$, $[I_c]$, and $[D_g]$ are highly relevant to granular velocity in terms of both linear and nonlinear measures.

5. Discussion

Hirzberger *et al.* (1997) invoked two different phenomena to explain why there is a weak concentration of small and faint granules in the downdrafts but a strong preponderance of large bright granules in the updrafts. First, the downdrafts are related to the edges of the supergranular flows, where small-scale magnetic fields are concentrated. These magnetic fields can produce a decrease in the size of the granulation pattern (Title *et al.*, 1992). Second, as for large and bright granules in the updrafts, they prefer to be located in the centers of the mesogranular upflows and may result from a strong similarity between exploding granules and mesogranules, as was found by Simon (1991). Furthermore, Simon (1991) also thought that the influence of magnetic field should be excluded and a strong relation between the large-scale flow field and the behavior of large and bright granules could be assumed.

In this article, we found that the granule-downflows are – on average – slightly smaller and fainter than the granule-upflows. Also, the flux densities of granule-downflows are slightly higher, and the Doppler velocity of lanes around these granules are also decreased. These conclusions can be explained with Hirzberger *et al.*'s (1997) idea. The granules in downflows are related to the edges of the supergranular flows. In the quiet Sun, the localized concentrations of intense vertical magnetic flux often accumulate in the convective downflows (Lin and Rimmele, 1999; Domínguez Cerdeña, Kneer, and Sánchez Almeida, 2003; Centeno *et al.*, 2007). Therefore, these granules may have strong magnetic-flux density.

In addition, we also found that the mean Doppler velocity of lanes is highly correlated with that of granules, as discussed in Section 4. This conclusion is inconsistent with some existing facts. It was claimed that the velocities in granular upflows are negatively correlated with the velocities in the surrounding lanes (Rast, 1995, 2003; Stein and Nordlund, 1998). Also, the fastest upflows are located close to the intergranular lanes (Nesis *et al.*, 1992; Hirzberger, 2002). In this work, the velocity we measured is the mean velocity within a granule and the intergranular lane. From panel (g) of Figure 3, we see these two mean velocities are positively correlated. We assume that at the size scale of granules and lanes,

these two velocities are positively correlated. They will be negatively correlated if the scale becomes greater. In order to verify this assumption, we compute the mean velocities of all of the granules and lanes at different scales, including 100×100, 500×500, and 900×900. Figure 6 shows that these two velocities are also positively correlated in square regions of 100×100 and 500×500 pixels. However, the relation of these two velocities becomes negatively correlated when we compute the mean velocities in a square region of 900×900 pixels. This is an interesting phenomenon, which is worth studying in the future.

6. Summary

We automatically identify 75 146 granules from the normal-mode observations of seven quiet regions by a marker-controlled watershed method. Eight properties of granules are measured. The distribution of the mean Doppler velocity within granules reaches a peak at -0.42 km s^{-1}. There are 55 226 (73.5%) granules with mean upward Doppler velocity (granule-upflows) and 19 920 (26.5%) granules with mean downward Doppler velocity (granule-downflows).

The statistical properties of granule-upflows and granule-downflows are studied, respectively. Granule-downflows are – on average – slightly smaller and fainter than granule-upflows. Also, the flux densities of granule-downflows are slightly higher.

The distributions of granule-upflows and granule-downflows are also analyzed. The continuum-intensity distribution of granule-upflows reaches a peak at 1.04, while that of granule-downflows reaches a peak at 0.99. The number of granule-upflows is greater than the number of granule-downflows if the transverse, absolute longitudinal, and unsigned flux density are less than 100 G, while the number of granule-upflows is less than the number of granule-downflows if the flux densities are greater than 100 G.

Moreover, we show that the Doppler velocity of lanes has the greatest correlation with the Doppler velocity of granules. The linear-correlation coefficient and the nonlinear relevance of these two parameters are the greatest. The linear-correlation coefficient is 0.61 computed by Pearson's correlation coefficient, and the nonlinear relevance is 0.18 measured with the mutual information. These two parameters are positively correlated.

Acknowledgements We are grateful to the *Hinode* team for providing the data. *Hinode* is a Japanese mission developed and launched by ISAS/JAXA, with NAOJ as a domestic partner and NASA and STFC (UK) as international partners. It is operated by these agencies in cooperation with ESA and NSC (Norway). We would also like to express our gratitude to Jun Zhang for useful discussions. This work is supported by the National Natural Science Foundations of China (10978011, 40870161, 11078010, and 61105054), the CAS Project KJCX2-YW-T04, the National Basic Research Program of China under grant G2006CB806303, and the National Science Fund for Distinguished Young Scholars under Grant 50925625.

References

Bahng, J., Schwarzschild, M.: 1961, *Astrophys. J.* **134**, 312.
Battiti, R.: 1994, *IEEE Trans. Neural Netw.* **4**, 537.
Berrilli, F., Del Moro, D., Florio, A., Santillo, L.: 2005, *Solar Phys.* **228**, 81.
Boomgaard, R., Balen, R.: 1992, *CVGIP, Graph. Models Image Process.* **54**, 252.
Bovelet, B., Wiehr, E.: 2001, *Solar Phys.* **201**, 13.
Brandt, P., Ferguson, S., Shine, R., Tarbell, T., Scharmer, G.: 1991, *Astron. Astrophys.* **241**, 1.
Centeno, R., Socas-Navarro, H., Lites, B., Kubo, M., Frank, Z., Shine, R., Tarbell, T.: 2007, *Astrophys. J.* **666**, 137.
Domínguez Cerdeña, I., Kneer, F., Sánchez Almeida, J.: 2003, *Astrophys. J.* **582**, 55.

Hirzberger, J.: 2002, *Astron. Astrophys.* **392**, 1105.
Hirzberger, J., Vazquez, M., Bonet, J., Hanslmeier, A., Sobotka, M.: 1997, *Astrophys. J.* **480**, 406.
Ichimoto, K., Lites, B., Elmore, D., Suematsu, Y., Tsuneta, S., Katsukawa, Y., Shimizu, T., Shine, R., Tarbell, T., Title, A.: 2008, *Solar Phys.* **249**, 233.
Jin, C., Wang, J., Zhao, M.: 2009, *Astrophys. J.* **690**, 279.
Keil, S.L., Canfield, R.C.: 1978, *Astron. Astrophys.* **70**, 169.
Kosugi, T., Matsuzaki, K., Sakao, T., Shimizu, T., Sone, Y., Tachikawa, S., Hashimoto, T., Minesugi, K., Ohnishi, A., Yamada, T.: 2007, *Solar Phys.* **243**, 3.
Lim, J.: 1990, *Two-Dimensional Signal and Image Processing*, Prentice-Hall, Englewood Cliffs, 710.
Lin, H., Rimmele, T.: 1999, *Astrophys. J.* **514**, 448.
Lites, B., Elmore, D., Streander, K., Akin, D., Berger, T., Duncan, D., Edwards, C., Francis, B., Hoffmann, C., Katz, N.: 2001, *Proc. SPIE* **4498**, 73.
Lites, B., Socas-Navarro, H., Kubo, M., Berger, T., Frank, Z., Shine, R.A., Tarbell, T.D., Title, A.M., Ichimoto, K., Katsukawa, Y., Tsuneta, S., Suematsu, Y., Shimizu, T.: 2007, *Publ. Astron. Soc. Japan* **59**, S571.
Lites, B., Kubo, M., Socas-Navarro, H., Berger, T., Frank, Z., Shine, R., Tarbell, T., Title, A., Ichimoto, K., Katsukawa, Y., Tsuneta, S., Suematsu, Y., Shimizu, T., Nagata, S.: 2008, *Astrophys. J.* **672**, 1237.
Meyer, F., Beucher, S.: 1990, *J. Vis. Commun. Image Represent.* **1**, 21.
Moga, A.N., Gabbouj, M.: 1998, *J. Parallel Distrib. Comput.* **51**, 27.
Nesis, A., Hanslmeier, A., Hammer, R., Komm, R., Matting, W., Staiger, J.: 1992, *Astron. Astrophys.* **253**, 561.
Ning, J., Zhang, L., Zhang, D., Wu, C.: 2010, *Pattern Recognit.* **43**, 445.
Rast, M.P.: 1995, *Astrophys. J.* **443**, 863.
Rast, M.P.: 2003, *Astrophys. J.* **597**, 1200.
Rivest, J., Soille, P., Beucher, S.: 2005, *Proc. SPIE* **158**, 139.
Roudier, T., Muller, R.: 1987, *Solar Phys.* **107**, 11.
Salembier, P., Pardas, M.: 1994, *IEEE Trans. Image Process.* **3**, 639.
Salembier, P., Marques, F.: 1999, *IEEE Trans. Circuits Syst. Video Technol.* **9**, 1147.
Schrijver, C.J., Hagenaar, H.J.: 1997, *Astrophys. J.* **475**, 328.
Shimizu, T., Nagata, S., Tsuneta, S., Tarbell, T., Edwards, C., Shine, R., Hoffmann, C., Thomas, E., Sour, S., Rehse, R.: 2008, *Solar Phys.* **249**, 221.
Simon, G.: 1991, *Astrophys. J.* **375**, 775.
Stein, R.F., Nordlund, A.: 1998, *Astrophys. J.* **499**, 914.
Suematsu, Y., Tsuneta, S., Ichimoto, K., Shimizu, T., Otsubo, M., Katsukawa, Y., Nakagiri, M., Noguchi, M., Tamura, T., Kato, Y.: 2008, *Solar Phys.* **249**, 197.
Sweldens, W.: 1998, *SIAM J. Math. Anal.* **29**, 511.
Title, A., Tarbell, T. (SOUP Team): 1986, *Bull. Am. Astron. Soc.* **18**, 661.
Title, A., Topka, K., Tarbell, T., Schmidt, W., Balke, C., Scharmer, G.: 1992, *Astrophys. J.* **393**, 782.
Tsuneta, S., Ichimoto, K., Katsukawa, Y., Nagata, S., Otsubo, M., Shimizu, T., Suematsu, Y., Nakagiri, M., Noguchi, M., Tarbell, T., Title, A., Shine, R., Rosenberg, W., Hoffmann, C., Jurcevich, B., Kushner, G., Levay, M., Lites, B., Elmore, D., Matsushita, T., Kawaguchi, N., Saito, H., Mikami, I., Hill, L.D., Owens, J.K.: 2008, *Solar Phys.* **249**, 167. doi:10.1007/s11207-008-9174-z
Yu, D.R., Xie, Z.X., Hu, Q.H., et al.: 2011, Astrophys. J. **740**, in press.